

Active Control and Optical Diagnostics of the Flow over a Hemispherical Turret

Bojan Vukasinovic, Ari Glezer,
*Woodruff School of Mechanical Engineering,
Georgia Institute of Technology, Atlanta, GA 30332-0405*

Stanislav Gordeyev, Eric Jumper,
*Department of Aerospace and Mechanical Engineering,
University of Notre Dame, Notre Dame, IN 46556*

Valdis Kibens
*The Boeing Company, MC S111-1240,
P.O. Box 516, St. Louis, MO 63166*

The effects of flow control actuation on the aerodynamic characteristics and aero optical distortions in the near wake of a hemispherical turret model were investigated in a series of wind tunnel experiments at $M = 0.3 - 0.64$. Flow control was applied using a spanwise array of high-frequency synthetic jet actuators oriented such that the long sides of their rectangular orifices were aligned in the streamwise direction. The effects of actuation on the flow dynamics and aero-optical distortions were characterized using Malley probe measurements, along with distributions of static surface pressure and hot-wire anemometry. One of the main findings of the present work was that the dissipative, small-scale motions that are induced by the actuation ($St_D > 1$) resulted in suppression of turbulent fluctuations within the separated flow over the hemisphere, and concomitantly in significant reduction in the levels of optical distortion (in excess of 40% at $M = 0.4$). The effect of the momentum limited actuation diminishes at $M > 0.45$.

Nomenclature

γ	= elevation angle
γ_a	= elevation angle of the actuators
γ_s	= separation angle
$\Delta\gamma_s$	= separation delay
ν	= kinematic viscosity
ρ	= freestream density
b_j	= actuator orifice width
C_μ	= jet momentum coefficient
D	= turret diameter
k	= turbulent kinetic energy
M	= Mach number
U_i	= i -component of the velocity
\overline{U}_i	= i -component of the mean velocity
u_i	= fluctuation of the i -component of the velocity
U_0	= free stream velocity
U_j	= average jet velocity
p	= static pressure
OPD	= optical path difference
OPD _{rms}	= root-mean-square of OPD
Re_D	= Reynolds number
St_D	= Strouhal number

I. Background

THE control of flow over a hemispherical turret being used as the housing for a laser-based optical system must satisfy more demanding requirements in comparison to separation control over an airfoil. Whereas the effectiveness of the flow control method on an airfoil can be evaluated strictly in terms of its effect on the time-averaged lift coefficient, the metric becomes much more stringent when the intent of flow control is to enhance transmission of optical wave fronts through regions of turbulent flow affected by potential separation. When an optical wavefront passes through a variable index-of-refraction turbulent flow, its wavefront gets distorted or aberrated. When the cause of these index-of-refraction variations is a relatively thin, of the order of meter or so region of the turbulent flow induced by the aircraft, it is referred as an *aero-optical problem*¹. These wavefront distortions combined with optical aberrations caused by the wavefront propagation through the atmosphere to a target (known as an *atmospheric propagation problem*²) ultimately degrade the light intensity from the otherwise diffraction-limited intensity at the target. Typical sources of aero-optical aberrations are turbulent boundary layers, separated shear layers and wakes. These aberrations have high spatial and temporal bandwidths which are well outside the capabilities of traditional adaptive-optic methods³. Separated shear layers are particularly destructive because of the presence of coherent vortical structures with their concomitant pressure/density wells inside them⁴. Left untreated, these shear-layer-related optical aberrations will limit an airborne transmitting system to a forward-looking quadrant only. In order to extend viewing angles to at least a portion of aft-looking quadrant, one can disrupt formation of the shear layer structure or extend the region of the attached flow by delaying the separation of the shear layer.

The intent of the work presented in this paper is to evaluate the effectiveness of a strategy for achieving significant improvement in light transmission efficiency by minimizing laser wavefront degradation through active flow control suppression of the unsteady aerodynamic environment that leads to beam degradation by the uncontrolled flow. Previous approaches to investigating an appropriate aircraft housing geometry to house a laser based system focused on the use of an aft-body fairing to achieve steady flow properties behind the weapon housing. This approach led to an extensive flight program using a KC-135A aircraft, configured as the Airborne Laser Lab (ALL, presently at the Air Force Museum in Dayton, Ohio). It was used in an 11-year experiment to demonstrate that high-energy lasers could be operated in an aircraft and employed against airborne targets.

The traditional active method for controlling separation behind two-dimensional airfoils makes use of the strong entrainment properties of a shear layer excited at its flapping frequency. Introducing perturbation signals at the nominal (dimensionless) frequency $St = O[1]$ upstream of the region of separation results in energizing the shear layer to a degree that results in the exhaustion of the air supply between the separated shear layer and the adjacent aerodynamic surface. This effect leads to a Coanda-like partial attachment of the separated flow to the aerodynamic surface. Once reattached, the flow responds to the modified pressure gradients along the surface, and typically separates again. The cycle of partial reattachment and separation repeats at a rate that is a low integer submultiple of the excitation frequency. While resulting in a considerable improvement in the mean lift coefficient associated with the affected surface, this method can degrade an optical signal that is transmitted through the affected region perhaps even beyond the levels observed if control were not applied. A body of work studying the control of separation by the application of perturbation signals at frequencies at least an order of magnitude higher than the flapping frequency of the shear layer suggests that such high-frequency excitation makes it possible to achieve attached flows that do not suffer the unsteady effects exhibited by traditional methods (e.g., Smith et al.⁵ and Amitay and Glezer⁶). The flows remain attached and the flow field is free of degrading optical effects of the periodic appearance of highly energized large-scale structures in the flow that is traversed by light waves.

Some previous work on separated flows over a three-dimensional bluff-body configuration has been directly motivated by the aero-optical problems involving an aircraft turret. Such a configuration typically consisted of a cylindrical base having a hemispherical cap and a flat or a conformal aperture. The resulting flow field is fairly complex as shown by de Jonckheere et al.⁷. The attempts at flow control of such flows were done by examining the effect of suction on the wake structure (Purohit et al.⁸) and by addition of aft-mounted fairings and splitter plates (Snyder et al.⁹). The former showed significant alteration of the wake structure even at low levels of suction, while the latter presented reduction of the baseline drag up to 55% using a large fairing. The separated flow behind the turret with the flat aperture and the effects of passive control on the optical aberrations were addressed and characterized by Gordeyev et al.¹⁰, while the aerodynamical and aero-optical characterization of the baseline flow field over the conformal-window turret configuration was recently investigated by Gordeyev et al.¹¹. Surprisingly enough, there is almost no work done on generic configuration of a flow over just a surface-mounted hemisphere at high Reynolds numbers, besides some motivated by Earth flows over hemispherical domes¹². In a numerical investigation of such a flow, Manhart¹³ found that Karman-like vortex train is shed from the hemisphere. In these flows however, the thickness of the upstream boundary layer is comparable to the hemisphere radius unlike the flow

over an aircraft turret for which the oncoming boundary layer thickness is much smaller than the turret radius. The effectiveness of direct, high-frequency control ($St_D > 10$) of the separated flow over a hemispherical turret on a flat plate with a thin upstream boundary layer was demonstrated by Vukasinovic et al.¹⁴ at $Re_D = 4 - 7 \times 10^5$. These authors showed that the presence of flow control can substantially reduce the extent of the recirculating domain downstream of the hemisphere with significant reduction in turbulent kinetic energy. Morgan and Visbal¹⁵ performed numerical investigation of the flow over a turret at $Re_D = 4.36 \times 10^5$ and $M = 0.5$, and compared a hybrid RANS/ILES and $k-\epsilon$ RANS simulations with experimental data for the baseline (uncontrolled) flow. Vukasinovic and Glezer¹⁶ demonstrated the effectiveness of fluidic, direct high-frequency control on turbulence suppression behind a bluff—body turret at $Re_D = 8 \times 10^5$.

The present paper extends our earlier work on the three-dimensional flow over a hemisphere¹⁴, on which the surface curves not only in the streamwise but also in the lateral direction and subjects the developing spanwise vorticity lines to distortion that makes the overall separation line complex. Synthetic jet actuators driven by high-frequency piezoelectric elements are used to explore the response of the separated region downstream of a hemispherical shell to variations in geometric distribution and primary and modulated frequency characteristics of an array of actuators. The metrics regarding flow quality and resulting changes in the optical transmission properties of the shear layer are defined and compared. Schematic of the global flow topology over a surface-mounted hemispherical turret is shown in Figure 1. The oncoming boundary layer at the flat surface rolls as it approaches adverse pressure induced by the bluff body; as the spanwise vortex lines become strained and deformed under the modified outer flow; this gives a rise to the streamwise vorticity, and as a consequence the wall flow swirls around in the downstream direction in a form of a necklace vortex. The outer flow is pushed away from the wall by the modified pressure field, and accelerates over the hemisphere surface until it encounters adverse pressure along the aft side, strong enough to induce separation off the hemisphere surface. Furthermore, the meridional pressure imbalance turns the separating flow inward, which causes the swirling off the hemisphere surface. The resulting separated bubble is nested in between the swirling “funnels” and consists of two recirculating domains that are merged at the plane of symmetry.

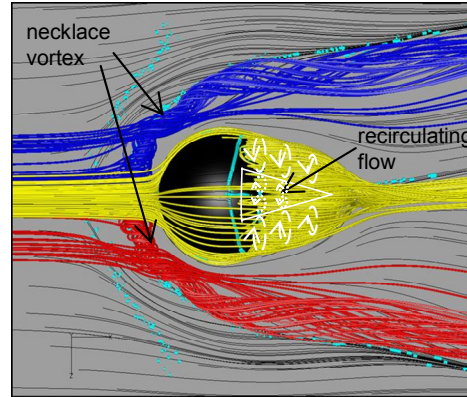


Figure 1. Schematics of flow separation over the hemispherical turret on a flat surface at low Mach number.

II. Experimental Setup and Procedures

The present experiments are conducted in the Trisonic Gasdynamics Facility (TGF) wind tunnel at Wright-Petersen AFB, a closed-return wind tunnel having a square test section that measures 61 cm on the side. The test section also has large optical window on one side, thus allowing a wide optical access. The hemispherical turret measured 10” in diameter and was assembled out of eight interchangeable segments. The hemispherical model was mounted on a splitter plate (Figure 2), thus providing the experimental condition that the thickness of the oncoming boundary layer was much smaller than the sphere radius, i.e., $\delta/R \ll 1$. One of the hemisphere segments, spanning 40° , had twelve piezo-electric actuators mounted from below, such that the actuator orifices were flush mounted on the hemisphere surface and aligned with the streamwise direction of the flow (Figure 2). Two orifices of each actuator module span about $\Delta\gamma = 9.5^\circ$ in the central plane, where elevation angle γ is measured relative to the horizon, as shown in Figure 2. The actuation angle γ_a was adjusted by disassembling and rearranging of the hemisphere

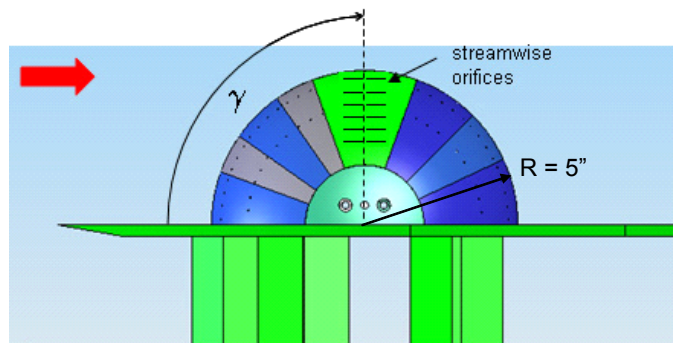


Figure 2. Side-view of the TGF hemisphere model equipped with a 40° actuator wedge comprised of twelve actuator modules across the span, having orifices aligned with the streamwise direction. Elevation angle γ is measured relative to the horizon.

segments.

Piezo-electric actuators (Figure 3) were custom designed and built such that each actuator module is compact and individually- addressed, and, upon actuation, it synthesizes a jet from the surrounding fluid¹⁷. The jet exits normal to the module's top plate through two jet orifices. Each of twelve actuator modules was calibrated prior to the experiments at a separate facility, and four jet velocities (defined as the mean jet velocity U_j of the expulsion part of the actuation cycle) were selected for the test runs. The hemisphere was also equipped with 96 pressure ports that were arranged in three rows: 36 ports were distributed along the central vertical plane, another 36 ports were aligned with the plane offset from the central by 20° , and 24 ports were distributed along the plane offset by 40° off the central plane.

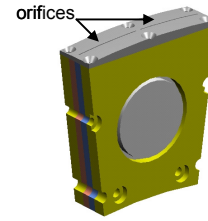


Figure 3. Schematics of the piezoelectric actuator module.

Both 20° -offset and 40° -offset pressure ports are visible on the side-view schematics shown in Figure 2. All pressure measurements were done using the dedicated computer and LabView-based DAQ. Besides static pressure measurements, spectral characterization of the flow was done by a miniature, single-sensor hot wire anemometry at a single downstream location $x/R = 1$ (where x is measured from the hemisphere center), and at different cross-stream locations y .

Experiments were run at four default free stream Mach numbers $M = 0.3, 0.4, 0.5$, and 0.64 . In addition to those, final measurements included $M = 0.45$ case, as present piezo-driven actuators showed decreasing effect in the range of $M = 0.4 - 0.5$. While the actuation (control) frequency was kept at optimal $f = 2000$ Hz, jet actuation strength was varied among four velocities. Also, the effect of an addition of low-frequency modulation f_{AM} (at the order of the expected shedding frequencies $St_{AM} \approx 0.2$) to the carrier high-frequency control signal was tested for three frequencies $f_{AM} = 100, 200$, and 400 Hz. After the optimal actuation parameters were determined, effect of actuation elevation angle γ_a was checked relative to the central separation point. For that purpose, two actuation angles were tested: $\gamma_a = 105^\circ$ and 110° .

Extensive measurements of the optical environment of the separated region behind the hemisphere without and with active flow control were conducted using Malley probe¹⁸. All measurements were taken along the centerplane aligned in the streamwise direction. Schematic of optical layout for Malley probe measurements is shown in Figure 4. Small, 5 mm diameter mirrors were mounted flush on the hemisphere along the centerline every 5 degrees at elevation angles of between 110 and 160 degrees, with the elevation angle of zero facing directly upstream. Two parallel Malley probe He-Ne laser beams separated in the streamwise direction were forwarded in the test section using series of steering mirrors and, after bouncing off the surface-mounted mirror were reflected back to the optical table exactly along the same optical path they were forwarded into. It allows the laser beams to go along the same measurement line twice, thus increasing signal-to-noise ratio and significantly simplifying the optical set-up. Five elevation angles were measured using the Malley probe: 120, 135, 140, 145 and 150 degrees. Optical aberrations at these angles were measured by recording instantaneous deflection angles of both laser beams using position sensing devices. Sampling frequency was 100 kHz, sampling time was 10 seconds.

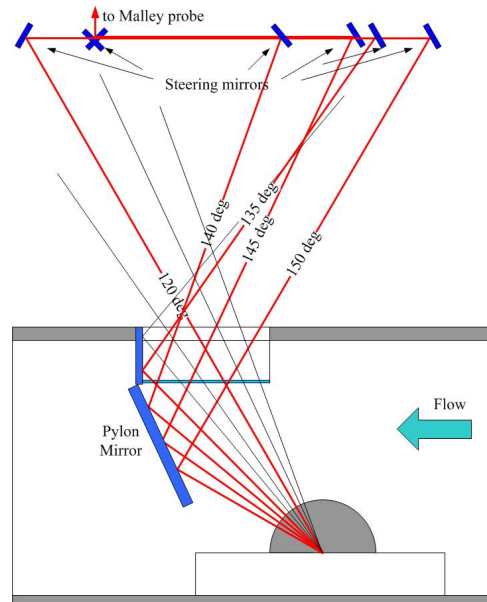


Figure 4. Schematic of optical measurements behind the hemisphere.

III. Baseline Flow

Baseline flows (without active flow control) are first characterized by surface static pressure measurements. The resulting pressure profiles along the centerline, 20° -off and 40° -off planes at $M = 0.3, 0.4, 0.5$, and 0.64 are shown in Figure 5. All profiles are plotted relative to the local elevation angle of the pressure port, i.e., in the central (γ_c), 20° -off (γ_m), and 40° -off (γ_o) planes. Pressure profiles in the central plane (Figure 5a) indicate that the flow separation point moves upstream with M , i.e., from just above 120° at $M = 0.3$ to about 115° at $M = 0.5$. A significant shift in the separation point at $M = 0.64$, where the flow separates just after the hemisphere apex is attributed to the localized

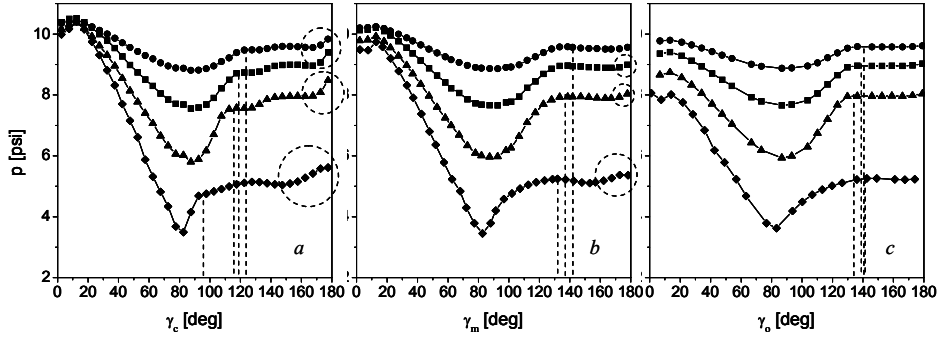


Figure 5. The static pressure distributions for the baseline flow at $M = 0.3$ (\bullet), 0.4 (\blacksquare), 0.5 (\blacktriangle), and 0.64 (\blacklozenge), along the central (a), 20° -off (b), and 40° -off (c) planes.

shock wave that develops in that region. It is also noteworthy that all four profiles exhibit pressure recovery towards the end (marked by a dashed circles), which is believed to be associated with the presence of the recirculating bubble. Pressure profiles in the 20° -off plane (Figure 5b) again indicate that the separation moves upstream with an increase in M , only this time the local elevation angle changes from just above 140° at $M = 0.3$ to just above 130° at $M = 0.64$. As horizontal projections of these points are downstream from the corresponding separation projections in the central plane, it appears that the flow stays attached longer in 20° -off plane than in the central plane in all cases. Besides, as the separation point at $M = 0.64$ is inline with the separation points at other Mach numbers, it is conjectured that the localized shock at the hemisphere apex does not spread up to the 20° -off plane. In addition, it can be seen that a pressure recovery towards the end of each profile is very mild, suggesting that the recirculating bubble weakened in the spanwise direction. Finally, baseline pressure profiles along the 40° -off plane are shown in Figure 5c. Although the local separation angles closely correspond to those in Figure 5b, the actual horizontal projections of these separation points are ahead of the corresponding ones in the 20° -off plane, and also closely trail the corresponding projections along the central plane. Therefore, even just these three separation points across the span indicate that the three-dimensional curvature of the hemisphere induces nonmonotonic separation line. Its complexity can be also enhanced by even minor manufacturing imperfections on the hemisphere surface or asymmetry of the oncoming flow. It should be also noted that there is virtually no additional pressure recovery past the separation points in 40° -off plane, suggesting that the recirculating bubble, which is present in the central zone behind the hemisphere, does not extend up to the 40° -off plane in the spanwise direction.

In addition to static pressure profiles, surface oil-flow visualization is used to elucidate the baseline flow topology. Figure 6a shows surface flow-visualization at $M = 0.3$ focused on the flow past the separation line. The flow footprint clearly indicates separation off the hemisphere surface that is symmetric relative to the plane of symmetry, having two “funneling” vortices, as already discussed in Figure 1. Contrary to such separation footprint, baseline flow at $M = 0.45$ (Figure 6b) exhibits asymmetric separation line, with additional distinct swirling motions. Also, a notable inward motion of the flow from the circumference is seen within the separated flow on the hemisphere surface. Besides the hemisphere surface flow visualization, Figure 6b also clearly visualizes the outer necklace vortex flow, as outlined in Figure 1. Overall, flow visualization at $M = 0.45$ is in accord with the surface flow visualization of the hemisphere-on-cylinder turret at comparable Mach number¹¹, while the low Mach number visualization illustrates symmetric flow topology outlined in Figure 1.

Results of the optical characterization of the baseline flow are shown in Figure 7 in terms of deflection

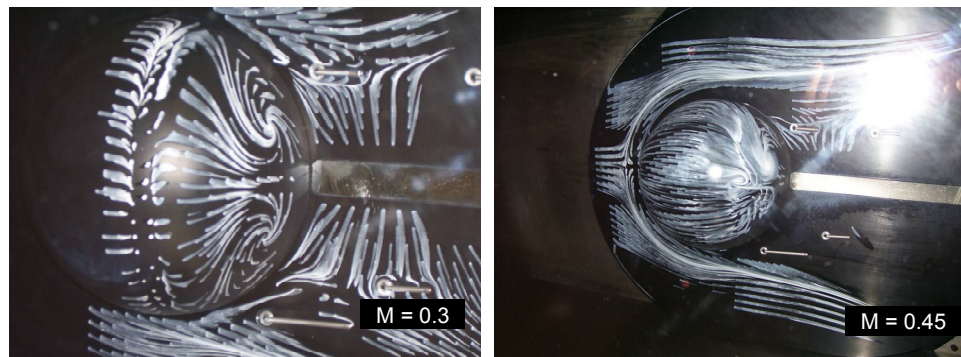


Figure 6. Surface oil-flow visualization of the baseline flows at $M = 0.3$ and 0.45 .

angle spectra for all measurement angles as a function of the elevation angle for different Mach numbers. Series of peaks at low frequencies below 0.8 kHz are a result of strong mechanical vibrations of the tunnel, the model and the pylon mirror. These vibrations completely overwhelm the optical signal at these frequencies and making data unusable at these frequencies. Above 0.8 kHz optical signal shows a broad hump which indicates the presence of the shear layer behind the hemisphere. The frequency location of this hump increases from approximately 1.5 kHz to 3 kHz with the Mach number increasing, as expected for the shear layer. Shear-layer-related spectra monotonically increases with the elevation angle increasing, indicating that the optical aberration caused by the shear layer gets stronger for increasing looking-back angles. Location of the shear layer peak moves toward smaller frequencies with the elevation

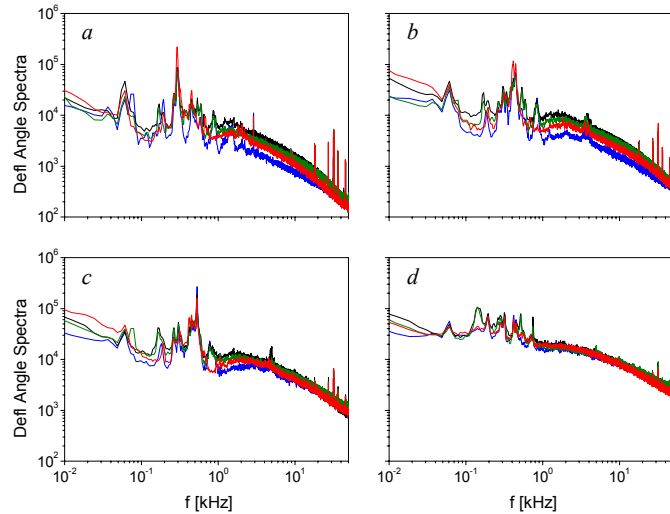


Figure 7. Optical deflection angle spectra for the incoming Mach numbers $M = 0.3$ (a), 0.4 (b), 0.5 (c), and 0.64 (d) as a function of elevation angles $\gamma = 120^\circ$ (—), 135° (—), 145° (—), and 150° (—).

angle increasing, from 2 kHz to 1.5 kHz for $M = 0.3$ and 0.4 and from 3 kHz to 2 kHz for $M = 0.5$. This is consistent with the shear layer structure growing in size downstream. Thus, two reasons the optical signal increases with the elevation angle are the shear layer structure growing downstream and the fact that the laser beam traverses through the shear layer at higher oblique angles and collecting more of optical aberrations along the path.

Compared with lower Mach number results, for $M = 0.64$ shear-layer related optical signal is quite stronger at this Mach number and only weakly depends on the elevation angle. As was mentioned before, at this Mach number the flow becomes supersonic on top of the hemisphere and creates an unsteady straight shock located on top of the hemisphere. This shock causes the boundary layer to separate prematurely over the hemisphere, thus creating the strong separation region for all looking-back angles. The same time it disrupts the shear layer formation, so large-scale structures are no longer present at looking-back angles and the only mechanism for increasing the optical signal is the oblique angle effect, discussed before.

A spectral cross-correlation technique¹⁸ was used to calculate a mean convective speed and to identify frequencies corrupted by mechanical vibrations. These mechanically-related vibrations can be seen as series of sharp peak below 0.8 kHz in deflection angle spectra in Figure 7. The low-pass filter with a cut-off frequency at 0.8 kHz was applied to remove mechanical vibration contamination from the deflection signals and levels of optical distortions, OPD_{rms} were computed for aperture of $3.33''$, as described in Ref. 14. Optical results are presented in Figure 8 in a self-similar form, $OPD_{rms}/(\rho M^2 D)$, versus the elevation angle for all Mach numbers. Also, the “oblique angle” effect, $OPD_{rms} \sim 1/\sin(\gamma)$ is shown in Figure 8 as a dashed line. For $M = 0.3$, 0.4 and 0.5 data collapse for the elevation angle of 150 degrees; for $M = 0.4$ and 0.5 collapse at 145 degrees. For low $M = 0.3$ data slightly deviate from the self-similar behavior right after the separation (elevation angles 135 and 145 degrees), indicating that flow at this Reynolds number is still transitional. When the flow goes supersonic on top of the hemisphere ($M = 0.64$), optical aberrations do not collapse with subsonic cases, but show higher levels of optical aberrations, as expected.

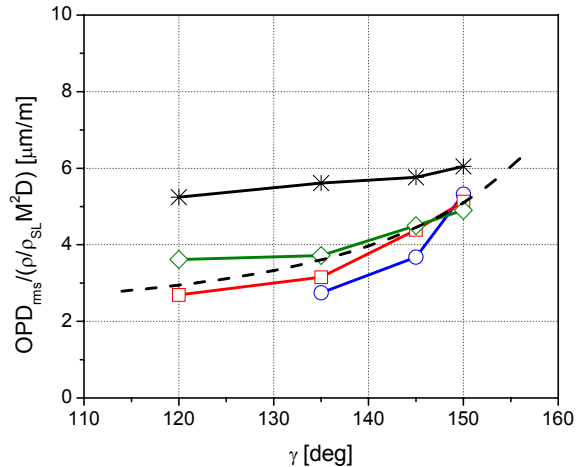


Figure 8. Normalized baseline OPD_{rms} for the incoming Mach numbers $M = 0.3$ (○), 0.4 (□), 0.5 (◇), and 0.64 (*) as a function of elevation angles. A line $1/\sin(\gamma)$ (---) is shown as a reference.

Summarizing, for $0.3 < M < 0.6$ and elevation angles above 130 degrees, levels of optical distortions imposed on laser beam can be approximately described as,

$$OPD_{rms} = 2.55 \times 10^{-6} \frac{\rho}{\rho_{SL}} \frac{M^2 D}{\sin(\gamma)},$$

where ρ_{SL} ($=1,225 \text{ kg/m}^3$) is the sea-level density. This empirical result can be used to estimate optical aberrations over hemispherical turrets for look-back elevation angles between 130 and 150 degrees for different altitudes (freestream density), Mach numbers and turret sizes.

IV. Flow Control

As preliminary tests showed that the favorable effect of active flow control on the delay in flow separation is directly proportional to the jet momentum coefficient, it is kept constant at the highest C_{μ} for the remainder of the tests. Furthermore, results presented in this section are focused on the actuation cases upstream from the separation ($\gamma_a = 110^\circ$ and 105°) as such relative location of the actuation is more likely to be encountered in practical applications, where it is expected that the flow separation will occur over the surface of the optical window.

The resulting static pressure profiles in terms of the pressure coefficient C_p are shown in Figure 9 for $\gamma_a = 110^\circ$ and four Mach numbers $M = 0.3, 0.4, 0.45,$ and 0.5 , in the central (γ_c), 20° -off (γ_m), and 40° -off (γ_o) planes. All pressure profiles are shown only over the elevation angle span downstream from the hemisphere apex, as actuation

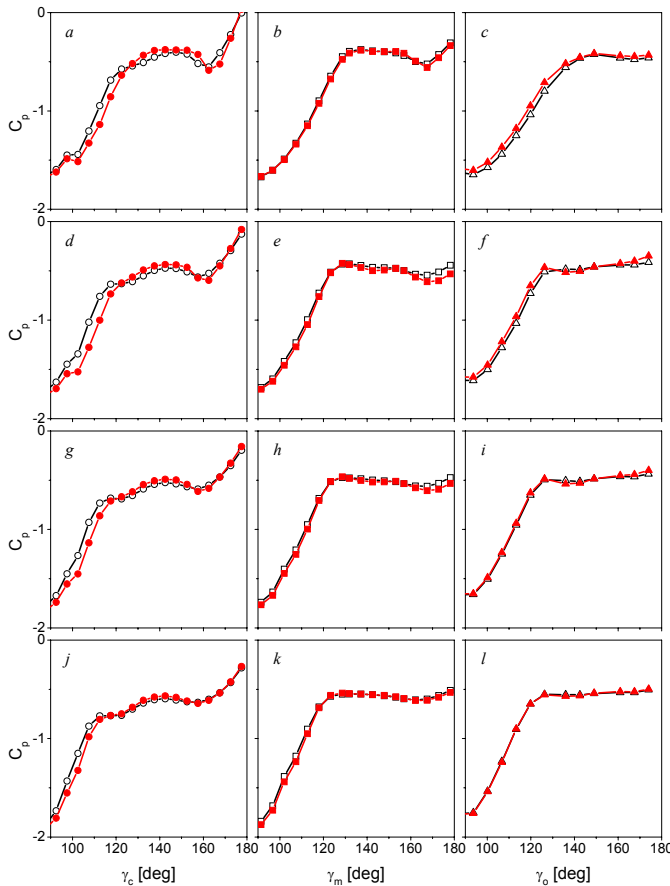


Figure 9. The static pressure distributions for the baseline (—) and actuated (—) flows along the central (a, d, g, j), 20° -off (b, e, h, k), and 40° -off (c, f, i, l) planes at $M = 0.3$ (a-c), 0.4 (d-f), 0.45 (g-i), 0.5 (j-l). Actuation angle is $\gamma_a = 110^\circ$.

does not alter the pressure profiles further upstream. Comparing the uncontrolled and controlled pressure profiles in the central plane for different Mach numbers, it becomes clear that the actuation effect weakens with the increase in M : after delaying separation for about 20° at $M = 0.3$ (Figure 9a) and 0.4 (Figure 9d), the separation delay significantly drops to about 5° at $M = 0.5$ (Figure 9j). It should be noted that the actuation angle was optimized for the actuation in the central plane, where the optical measurements are taken. This resulted in no significant alteration of pressure profiles in other two planes, which is attributed to the non-optimal distance between the actuation orifices and local separation points. However, favorable effect of the high-frequency control on suppression of fluctuating motions in separated flows is twofold: a) by virtual aeroshaping of the flow boundary that delays flow separation and b) by direct and active disruption of turbulent kinetic energy budget by dissipative mechanisms¹⁹. Therefore, the impact on turbulent kinetic energy suppression in the wake can be achieved even in the absence of significant separation delay.

Deflection angle spectra presented in Figure 10 have shown that the actuation reduces optical aberrations for all frequencies above 0.8 kHz at Mach number of 0.4 . An actuation peak at 2 kHz from the actuation can be seen as a small spike in all actuation spectra in Figure 10. The actuation at 110 degrees was found to reduce optical aberrations at $M =$

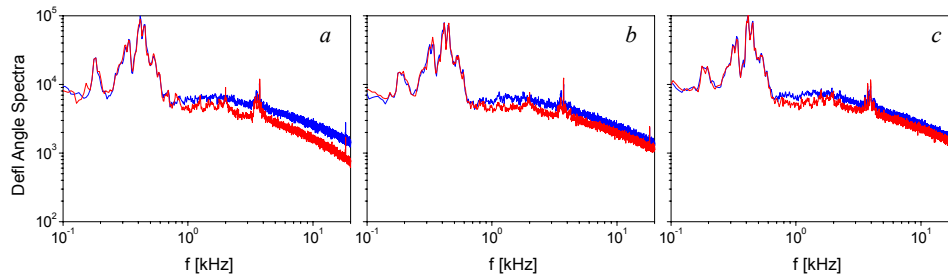


Figure 10. Optical deflection spectra for baseline (—) and actuation (—) cases at $\gamma_a = 110^\circ$ degrees at elevation angles $\gamma = 140^\circ$ (a), 145° (b), and 150° (c). Incoming $M = 0.4$.

0.45 (not shown), as well as to extend the improving effect at elevation angles up to 150 degrees. At $M = 0.5$ the actuation was found to be not strong enough to improve the optical characteristics of the flow. Summary of optical results are presented in Table 1. The actuation at 110 degrees indeed improves optical environment, reducing levels of optical distortion by approximately 40 % for $M = 0.4$ at the elevation angle of 140 degrees and by roughly 20% for a higher elevation angle of 150 degrees. For higher Mach numbers of 0.45 and 0.5 actuation at the elevation angle of 140 degrees the effect diminishes, dropping to a modest 10% improvement in optical aberrations at $M = 0.45$ and showing virtually no optical improvement for $M = 0.5$.

Table 1. OPD_{rms} (microns) for baseline and actuation at 110 degrees
(first number – baseline, second – actuation, third – relative reduction in OPD_{rms})

Elevation Angle, γ (deg)	M=0.3	M=0.4	M=0.45	M=0.5
140	0.051	0.101	0.132	0.161
	0.035	0.059	0.123	0.158
	(0.69)	(0.58)	(0.93)	(0.98)
145	--	0.099	--	--
	--	0.071	--	--
150	--	(0.72)	--	--
	--	0.116	--	--
	--	0.090	--	--
	--	(0.78)	--	--

To check how sensitive the impact of fluidic control origin on the resulting flow field is, actuation angle is then changed to $\gamma_a = 105^\circ$, and a new set of flow characterization was conducted, including the optical measurements. The resulting pressure profiles are plotted in Figure 11 for the flows at $M = 0.4, 0.45,$ and 0.5 , and along the same three measurement planes. Similar separation delay results relative to $\gamma_a = 110^\circ$ in the central plane are measured, with also more visible effects in other two measurement planes. It should be noted that similarity of the control effects at two actuation angles ($\gamma_a = 105^\circ$ and 110°) also implies that the control effect is not too sensitive to the location of the control source, which adds to the robustness of this control tool.

In addition to the static surface-pressure measurements, spectral characterization of the separated flow with and without active flow control was done using the hot-wire anemometry that corresponds to the flow and actuation conditions presented in Figure 11a in terms of the pressure profiles. Six such power spectra for the unforced (baseline) and forced (controlled) flows are shown in Figure 12, measured at $x/R = 1$ and six elevation coordinates y that correspond to $y/R = 0.3, 0.4, 0.6, 0.7, 0.75,$ and 0.8 . At the location closest to the splitter plate (Figure 12a), there is the lowest overall level in fluctuation energy of the baseline flow, and actuation suppresses some of the energy at the largest scales, up to 100 Hz. As the measurement point moves towards the shear layer, the effect of the actuation becomes less pronounced up to the point at $y/R = 0.6$ (Figure 12c), where there is no noticeable spectral effect of the actuation. However, once the measurement point starts moving through the shear layer (Figures 12d-f), a clear drop in broadband spectral energy is detected. Furthermore, the broadband suppression becomes more pronounced with the increase in elevation, which is a direct consequence of the convection of the high-frequency actuation through the shear layer. It should be noted also that the high-frequency effect weakens in the downstream

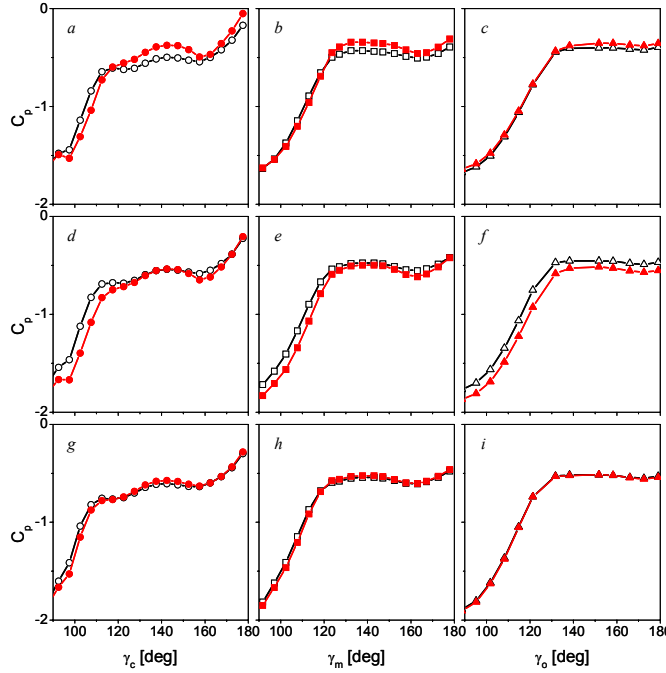


Figure 11. The static pressure distributions for the baseline (—) and actuated (—) flows along the central (a, d, g), 20°-off (b, e, h), and 40°-off (c, f, i) planes at $M = 0.4$ (a-c), 0.45 (d-f), and 0.5 (g-i). Actuation angle is $\gamma_a = 105^\circ$

direction due to inherit dissipation of direct high-frequency motions that are imposed onto the flow at the control origin.

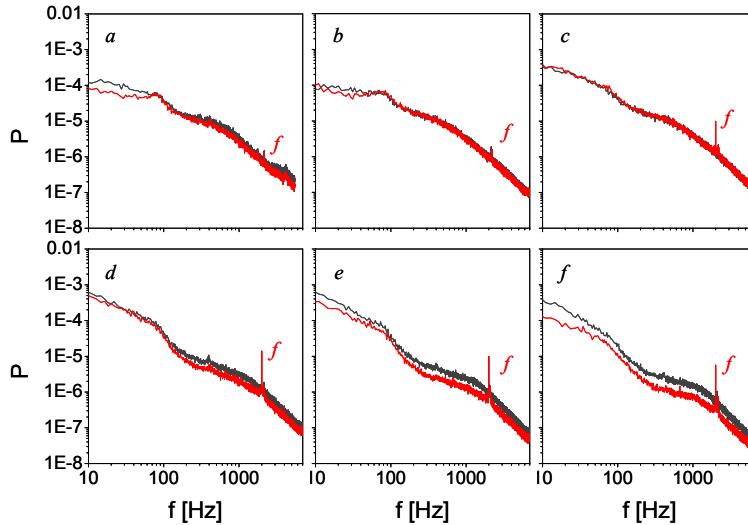


Figure 12. Power spectra of the velocity fluctuations for the $M = 0.4$ baseline (—) and the flow actuated at $St = 3.73$ (—) at $x/R = 1$ and $y/R = 0.3$ (a), 0.4 (b), 0.6 (c), 0.7 (d), 0.75 (e), and 0.8 (f).

Deflection spectra for different elevation angles for baseline and the actuation at 105 degrees for $M = 0.4$ are shown in Figure 13 and the summary of OPD_{rms} is presented in Table 2. As before, actuation frequency can be seen at all actuation spectra at 2 kHz in Figure 13. Improvements in the optical environment using the actuation are quite similar, but slightly weaker than the results as the actuation at 110 degrees, see Figure 10 and Table 1, respectively. It can be attributed to the fact that the actuators are located further upstream from the separation line and have slightly lesser effect on the separated shear layer.

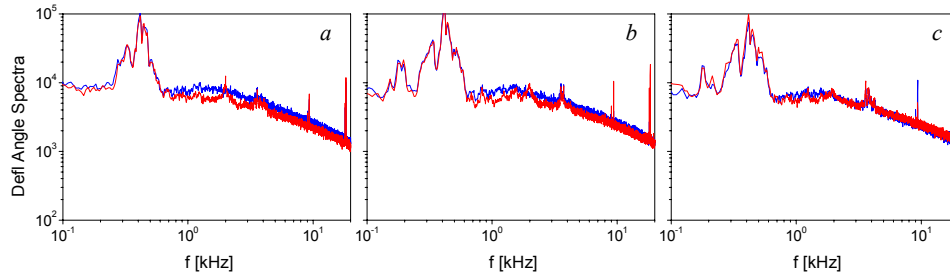


Figure 13. Optical deflection spectra for baseline (—) and actuation (—) cases at $\gamma_a = 105$ degrees at elevation angles $\gamma = 135^\circ$ (a), 140° (b), and 150° (c). Incoming $M = 0.4$.

Table 2. OPD_{rms} (microns) for baseline and actuation at 105 degrees
(first number – baseline, second – actuation, third – relative reduction in OPD_{rms})

Elevation Angle (deg)	M=0.4	M=0.45	M=0.5
135	0.082	0.123	0.151
	0.075	0.111	0.143
140	(0.91)	(0.90)	(0.95)
	0.104	--	--
150	0.073	--	--
	(0.70)	--	--
150	0.106	--	--
	0.090	--	--
	(0.85)	--	--

Besides continuous high-frequency actuation, the effect of addition of low-frequency modulation of the carrier high-frequency actuation is also applied as a control signal in order to check the flow receptivity to simultaneous direct high-frequency forcing and indirect excitation of organized motions at large scales. The modulation frequency f_{AM} was selected to be at the order of expected shedding frequencies off the hemisphere surface ($St_{AM} \approx 0.2$). Three such frequencies were tested, $f_{AM} = 100, 200,$ and 400 Hz, and characteristic central pressure profiles that correspond to such actuated cases are shown in Figure 14 for $M = 0.4$. In any of the cases, there is a negligible effect on the static pressure profiles, and, consequently, on the separation point. This can be in part contributed to the fact that amplitude-modulation of the carrier signal by a square-wave signal at f_{AM} and 50% duty cycle, halves the effective jet momentum coefficient relative to the non-modulated signal, which has a significant impact on the flow separation (Figure 9).

Previous studies¹⁴ suggested that, as the separated flow is receptive to f_{AM} frequencies, coherent motions at those frequencies were induced in the flow, thereby actively demodulating the modulated control input. To check the spectral content of the baseline and the flow actuated by modulated control input, hot-wire measurements were taken

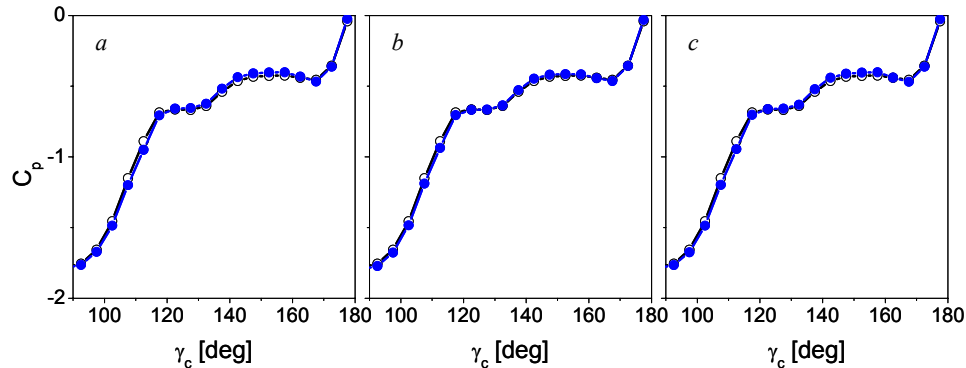


Figure 14. The static pressure distributions for the baseline (\circ , $M = 0.4$) and the flow actuated at $St = 3.73$, amplitude-modulated (\bullet) at $St_{AM} = 0.187$ (a), 0.373 (b), and 0.746 (c).

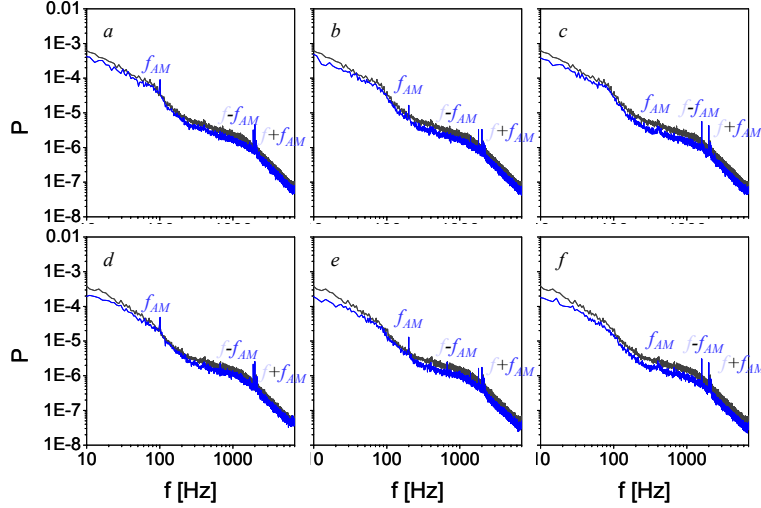


Figure 15. Power spectra of the velocity fluctuations for the $M = 0.4$ baseline (\blackrightarrow) and the flow actuated at $St = 3.73$ at $x/R = 1$ and $y/R = 0.75$ (a–c), and 0.8 (d–f), amplitude-modulated (\bluearrow) at $St_{AM} = 0.187$ (a, d), 0.373 (b, e), and 0.746 (c, f).

at the downstream hemisphere edge ($x/R = 1$) and several cross-stream elevations y . Representative results are shown in Figure 15 for the flow at $M = 0.4$ and $y/R = 0.75$ and 0.8 , and modulation cases $f_{AM} = 100, 200,$ and 400 Hz, which correspond to $St_{AM} = 0.187, 0.373,$ and 0.746 , respectively. First notable feature of all modulation cases shows that there is a broadband reduction in the energy content of the fluctuating velocity component. This suggests that although there is no significant change in the separation delay (cf. Figure 12), the high-frequency component of the amplitude-modulated control signal still suppresses turbulent kinetic energy of the separated flow. These findings support the assertion that the favorable effect of the high-frequency control on suppression of fluctuating motions in separated flows is twofold, and that direct and active disruption of turbulent kinetic energy budget results via dissipative mechanisms even in the absence of significant separation delay. Also, it is obvious from each power spectrum in Figure 15 that modulation control signal is actively demodulated by the flow, as coherent motions at f_{AM} are detected by spectral peaks in Figures 15a–c at the corresponding modulation frequencies. Besides the broadband reduction in energy, all spectra exhibit spectral peaks at $f - f_{AM}, f,$ and $f + f_{AM}$, which are the signatures of the control signal. The remaining peak at f_{AM} signals the induced large-scale motion at the modulation frequency, which is indirectly excited in the flow by amplitude-modulated, high-frequency control signal.

V. Conclusions

Present work was focused on experimental investigation of the high-frequency fluidic flow control on the separated flow over a hemispherical turrets at free stream speeds up to $M = 0.64$. Flow characterization included surface static pressure measurements, hot-wire anemometry and optical Malley probe measurements. Fluidic flow control was effected by a meridional array of synthetic jet actuators flush-embedded into the hemisphere surface, having the orifices aligned with the free stream direction. Besides a pure excitation of small-scale motions at the control origin, concomitant excitation of small- and large-scale motions is also effected via amplitude-modulation of the high-frequency control signal.

Present flow and optical measurements show that high-frequency, dissipative actuation can lead to broadband suppression of flow fluctuations within the near wake and, consequently, to improvement in aero-optical aberrations. It is shown that the current set of actuators imposed a notable active separation delay in the central domain of the turret up to $M \approx 0.45$, with a decrease in effectiveness as M increases. In any case of the imposed delay in separation due to the high-frequency control, analysis of the optical Malley probe measurements shows that the active flow control both delays the separation and reduces the magnitude of the phase gradient within the shear layer vortices, with visibly improved optical aberrations up to the elevation angle $\gamma = 150^\circ$, having levels of optical distortions reduced in excess of 40% at $M = 0.4$. As the Mach number further was increased, the reduction of optical distortions dropped down to a couple of percents at $M = 0.5$, which is partially attributed to the momentum limitations on the current generation of actuators. Furthermore, it should be noted that local Mach numbers at the synthetic jet actuation are actually higher than in the free stream flow. It is expected that the ongoing design of the

new generation of actuators will extend significant suppression of optical distortions into higher Mach-number flows. It is important to note that similar results were obtained in both fluidic and optical measurements of flows actuated at two actuation angles $\gamma_a = 105^\circ$ and 110° , which implies that the effect of high-frequency control is not very sensitive to the actuation location (within a range). Still, both fluidic and optical measurements suggest similar, but slightly better results for the actuation at $\gamma_a = 110^\circ$ than at $\gamma_a = 105^\circ$ in terms of reduction of levels of optical distortion. For instance, actuation at $\gamma_a = 110^\circ$ yields reduction of optical distortion of 42%, while actuation at $\gamma_a = 105^\circ$ yields the 30% reduction at the elevation angle of $\gamma = 140^\circ$. Also, reduction in optical distortions of 5% is measured for the flow at $M = 0.5$ for the actuation at $\gamma_a = 105^\circ$. Complementary spectral measurements by the hot-wire anemometry indicate that overall reduction in broadband energy of fluctuating velocity accompanies measured reduction in optical aberrations.

Besides the pure harmonic actuation of the separated flow, present study also explored a concomitant excitation of small- and large-scale motions in the forced flow by indirect excitation of large-scale motion via amplitude-modulation of the control signal. The results of that study suggested that no separation delay was imposed by the fluidic control. In spite of that, a broadband suppression of velocity fluctuations was still measured by the hot-wire anemometry, and such findings support the assertion that not only virtual aeroshaping of the flow boundary, but also direct dissipative suppression is the mechanism that is responsible for the reduction in overall turbulent kinetic energy in the separated flow, when an active, high-frequency flow control is applied. Also, it is found that large-scale coherent motions at the modulation frequency were present in the actuated flow, along with the expected sidebands of the high-frequency carrier. Along with previous studies¹⁴, these findings suggest that amplitude-modulation of the harmonic control signal should be further explored in pursuit of the “flow regularization” of the separated flow, where organized motions at known frequency and phase can be “seeded” into the flow, along with the benefits of reduced turbulent kinetic energy levels owing the dissipative effect of the high-frequency (carrier) actuation.

Acknowledgment

This work has been supported by the Air Force Research Laboratory and the Boeing Company.

References

- ¹Gilbert, J. and Otten, L. J. (eds), *Aero-Optical Phenomena*, Progress in Astronautics and Aeronautics, Vol. 80, AIAA, New York, 1982.
- ²Tatarskii, V. I. and Zavorotnyi, V. U., “Wave propagation in random media with fluctuating turbulent parameters,” *J. Opt. Soc. Am. A*, Vol. 2, No. 12, 1985, pp. 2069-2076.
- ³Jumper, E. J., and Fitzgerald, E. J., “Recent advances in aero-optics,” *Progress in Aerospace Sciences*, Vol. 37, 2001, pp.299-339.
- ⁴Fitzgerald, E. J. and Jumper E. J., “The optical distortion mechanism in a nearly incompressible free shear layer,” *J. Fluid Mech.*, Vol. 512, 2004, pp. 153-189.
- ⁵Smith, D. R., Amitay, M., Kibens, V., Parekh, D., and Glezer, A., “Modification of lifting body aerodynamics using synthetic jet actuators,” *AIAA Paper* 1998-0209, 1998.
- ⁶Amitay, M. and Glezer, A., “Role of actuation frequency in controlled flow reattachment over a stalled airfoil,” *AIAA Journal*, Vol. 40, 2002, pp.209-216.
- ⁷de Jonckheere, R., Russell, J. J., and Chou, D. C., “High subsonic flowfield measurements and turbulent flow analysis around a turret protuberance,” *AIAA Paper* 82-0057, 1982.
- ⁸Purhoit, S. C., Shang, J. S., and Hankey, W. L., “Effect of suction on the wake structure of a three-dimensional turret,” *AIAA Paper* 83-1738, 1983.
- ⁹Snyder, C. H., Franke, M. E., and Masquelier, M. L., “Wind-tunnel tests of an aircraft turret model,” *J. Aircraft*, Vol. 37, 2000, pp. 368-376.
- ¹⁰Gordeyev, S., Jumper, E. J., Ng, T. T., and Cain, A. B., “The optical environment of a cylindrical turret with a flat window and the impact of passive control devices,” *AIAA Paper* 2005-4657, 2005.
- ¹¹Gordeyev, S., Post, M. L., McLaughlin, T., Ceniceros, J., and Jumper, E. J., “Aero-optical environment around a conformal-window turret,” *AIAA J.*, Vol. 45, 2007, pp. 1514-1524.
- ¹²Toy, N., Moss, W. D., and Savory, E., “Wind tunnel studies on a dome in turbulent boundary layers,” *J. Wind Eng. Ind. Aerodynamics*, Vol. 11, 1983, pp. 201-212.
- ¹³Manhart, M., “Vortex shedding from a hemisphere in a turbulent boundary layer,” *Theoret. Comput. Fluid Dynamics*, Vol. 12, 1998, pp. 1-28.

- ¹⁴Vukasinovic, B., Brzozowski, D., Glezer, A., Bower, W., and Kibens, V, "Separation control over a surface-mounted hemispherical shell", *AIAA Paper 2005-4878*, 2005.
- ¹⁵Morgan, P. E. and Visbal, M. R., "Numerical investigation of flow around a turret", *AIAA Paper 2007-4480*, 2007.
- ¹⁶Vukasinovic, B. and Glezer, A., "Control of a separating flow over a turret", *AIAA Paper 2007-4506*, 2007.
- ¹⁷Smith, B.L. and Glezer, A., "The Formation and Evolution of Synthetic Jets", *Phys. Fluids*, Vol. 10, 1998, pp. 2281 – 2297.
- ¹⁸S. Gordeyev, T. Hayden and E. Jumper, "Aero-Optical and Flow Measurements Over a Flat-Windowed Turret", *AIAA Journal*, Vol. 45, pp. 347-357, 2007.
- ¹⁹Vukasinovic, B., Glezer, A., and Rusak, Z., "Experimental and numerical investigation of controlled, small-scale motions in a turbulent shear layer", *Proc. 3rd International Symposium of Integrating CFD and Experiments in Aerodynamics*, June 2007, U.S. AFA, CO, USA.